ACS ES&T Air

pubs.acs.org/estair

Article



# Relative Humidity Modulates the Physicochemical Processing of Secondary Brown Carbon Formation from Nighttime Oxidation of Furan and Pyrrole

*Published as part of ACS ES&T Air virtual special issue "Wildland Fires: Emissions, Chemistry, Contamination, Climate, and Human Health".*

Kunpeng Chen, Caitlin Hamilton, Bradley Ries, Michael Lum, Raphael Mayorga, Linhui Tian, Roya Bahreini, Haofei Zhang, and Ying-Hsuan Lin*

Cite This: ACS EST Air 2024, 1, 426−437

Read Online

ACCESS | Metrics & More | Article Recommendations | Supporting Information

**ABSTRACT:** Light-absorbing secondary organic aerosols (SOAs), also known as secondary brown carbon (BrC), are major components of wildfire smoke that can have a significant impact on the climate system; however, how environmental factors such as relative humidity (RH) influence their formation is not fully understood, especially for heterocyclic precursors. We conducted chamber experiments to investigate secondary BrC formation from the nighttime oxidation of furan and pyrrole, two primary heterocyclic precursors in wildfires, in the presence of pre-existing particles at RH < 20% and ∼ 50%. Our findings revealed that increasing RH significantly affected the size distribution dynamics of both SOAs, with pyrrole SOA showing a stronger potential to generate ultrafine particles via intensive nucleation processes. Higher RH led to increased mass fractions of oxygenated compounds in both SOAs, suggesting enhanced gas-phase and/or multiphase oxidation under humid conditions. Moreover, higher RH reduced the mass absorption coefficients of both BrC, contrasting with those from homocyclic precursors, due to the formation of non-absorbing high-molecular-weight oxygenated compounds and the decreasing mass fractions of molecular chromophores. Overall, our findings demonstrate the unique RH dependence of secondary BrC formation from heterocyclic precursors, which may critically modulate the radiative effects of wildfire smoke on climate change.

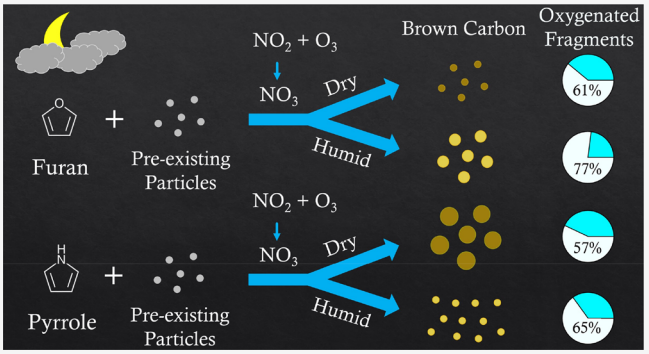


**KEYWORDS:** *furan and pyrrole, secondary organic aerosols, size distribution dynamics, oxygenated compounds, molecular chromophores*

## INTRODUCTION

Light-absorbing aerosols from wildfires can affect the climate system by directly heating the atmosphere and indirectly altering the aerosol-boundary-layer-monsoon interactions.[1−3] Over the last few decades, climate change has increased the intensity and frequency of wildfires,[4−6] releasing a massive amount of volatile organic compounds (VOCs) and aerosols into the atmosphere.[7−9] However, the impact of unabated wildfire emissions is highly uncertain due to the less-constrained radiative effects of wildfire smoke, which are influenced by the composition of smoke aerosols. The major component of smoke aerosols is organics (>95%),[10,11] contributing to ∼45−86% of the total aerosol light absorption.[12] A large fraction of smoke organics (∼30−56%) accounts for secondary organic aerosols (SOAs),[13] in which the light-absorbing component is known as secondary brown carbon (BrC). Thus, secondary BrC plays a critical role in moderating the climate impacts of wildfire smoke.

The formation of secondary BrC can be sensitive to the smoke environments.[14,15] In particular, relative humidity (RH) is a well-known environmental factor that may alter SOA composition and secondary BrC light absorption. Extensive research has revealed that changes in RH can influence SOA formation by altering the gas-phase chemistry, gas-to-particle partitioning of oxidation products, phase states of aerosols, reactive uptake of radicals, and heterogeneous reactions of

Received: February 7, 2024
Revised: April 4, 2024
Accepted: April 4, 2024
Published: April 9, 2024

aerosol-phase constituents.[16−27] Prior studies also reported that higher RH increased the mass absorption coefficients (MAC) of secondary BrC derived from homocyclic aromatic precursors.[28−30] The increased MAC was associated with changes in molecular chromophores as RH increased, which may alter the wavelength dependence of MAC profiles.[30] On the other hand, higher RH decreased the MAC of secondary BrC derived from $\alpha$-pinene,[31] suggesting that the effect of RH on MAC may differ depending on the type of VOCs. It is noted that a rise in RH may result in increased liquid water content in wildfire aerosols, where water-soluble organics can contribute to a large portion (e.g., ∼45% at 405 nm) of BrC light absorption.[32] Despite the extensive investigations, the effect of RH on secondary BrC formation remains inconclusive.

Heterocyclic VOCs are the second largest sources of wildfire SOA precursors, and they are more reactive compared to homocyclic VOCs (e.g., phenolics) due to their hetero atoms.[33,34] Common heterocyclic VOCs released by wildfire include furans and pyrroles,[34−37] which account for ∼30% of nitrate radical ($NO_3$) loss via nighttime chemistry in wildfire plumes.[38] Furans have greater emission factors but may generate less-absorbing BrC from nighttime chemistry, whereas pyrroles exhibit the opposite behavior.[35,36,39,40] Secondary BrC formation from the nighttime chemistry of furans and pyrroles has been widely studied under RH conditions below 20%,[14,15,39−41] a typical level in dry wildfire smokes (e.g., the Williams Fire smoke[42]) or dry fire areas (e.g., western United States[43,44] and Africa in dry seasons[45,46]). In addition, there have been frequent observations of humid wildfire smoke worldwide, particularly those at RH ∼50%, in the past two decades due to climate change.[47−49] A prior study of secondary BrC from indole, which contains a pyrrole ring in its structure, highlighted that the effects of RH on the light absorption properties of secondary BrC from heterocyclic VOCs were complicated and greatly unconstrained.[50] Hence, there was still a significant lack of process-level understanding regarding the secondary BrC formation from heterocyclic VOCs at various levels of RH.

In this study, chamber experiments were conducted to investigate the effects of RH on the secondary BrC formation from the nighttime oxidation of furan and pyrrole, the backbone compounds of furans and pyrroles. For comparison, RH was controlled at <20% and ∼50% to simulate dry and humid environments, respectively, while pre-existing particles were introduced in both RH so that the chamber conditions would be closer to the ambient atmosphere. The effects of RH on particulate size distribution dynamics, SOA composition, BrC light absorption properties, and molecular chromophores were examined to better understand how RH-related physicochemical processing modulates the secondary BrC formation from furan and pyrrole and their implications in the atmosphere. These results will provide more accurate representations of wildfire-associated secondary BrC and aid in assessing their climate impacts.

## METHODS

**Chamber Experiments.** All the experiments were carried out in a 10 $m^3$ Teflon fluorinated ethylene propylene (FEP) film chamber at room temperature (20−25 °C) under dark conditions. The room temperature was much lower than the temperature of wildfires but comparable to the temperature of ambient atmosphere,[47,49,51] where furan and pyrrole released from wildfires were observed in field studies.[34,37] Temperature and RH were monitored by a RH-USB sensor (Omega Engineering, Inc.) attached to the chamber. A constant output atomizer (TSI 3076) was used to produce pre-existing particles using a 10 mM ammonium sulfate ($(NH_4)_2SO_4$, Acros Organics, 99%, extra pure) solution. The pre-existing particles had a mass concentration and the central diameter of ∼50 $\mu g\ m^{-3}$ and ∼50 nm, respectively, to simulate the background particles in wildfire smoke.[52,53] Given that higher RH can introduce liquid water or increase the amount of liquid water content in wildfire aerosols,[48,54] we generated dry pre-existing particles at RH <20% and wet aqueous pre-existing particles at RH ∼50%. Because our humid condition was between the efflorescence RH and deliquescence RH of ammonium sulfate,[55] dry seed particles were produced by passing through a silica-gel filled diffusion dryer, whereas wet aqueous seed particles were produced without the dryer.[56] Chamber experiments without pre-existing particles were also performed at both RH levels. These experiments serve as a benchmark for detailed discussions on the potential mechanisms involved in SOA formation.

This study used furan (TCI America, >99%) and pyrrole (TCI America, >99%) as model compounds of heterocyclic VOCs. Each experiment involved only one VOC, in which ∼200 ppbv of furan or pyrrole was injected into the chamber using ∼15 lpm of zero air. The concentration of VOCs was determined based on previous studies to ensure appropriate SOA mass concentrations for online and offline analyses.[14,15,40,41] After 20 min of mixing, a mixture of $NO_2$ and $O_3$ (molar concentration ratio ∼3:2) was injected into the chamber, wherein $N_2O_5$ was generated and then decomposed to $NO_3$ radicals. $O_3$ was generated by an $O_3$ generator (A2Z Ozone 3G LAB) with pure oxygen (flow rate of 0.2 lpm), while $NO_2$ was directly injected from a $NO_2$ cylinder (4789 ppm, Airgas) with a flow rate of 0.5 lpm. Similar to prior studies of SOA formation under humid conditions,[20,21] the $NO_2$−$O_3$ ratio ensured that $NO_3$ primarily drove the oxidation of pyrrole and furan in our chamber. The $NO_2$−$O_3$ mixture was first reacted in a glass vessel (total flow rate of 0.7 lpm and residence time of 206 s) before the chamber injection. The concentration of $N_2O_5$ produced in the glassware was estimated by modeling the reactions between $NO_2$ and $O_3$, and the initial concentration ratio of $N_2O_5$ to furan (or pyrrole) was approximately 2:1. While it was possible that $O_3$ residue was also introduced into the chamber along with $N_2O_5$, the reaction rate constants ($k$) at room temperature and atmospheric pressure for "furan/pyrrole + $NO_3$" ($k_{furan+NO3}$ = $1.4 \times 10^{-12}$ $cm^3$ $molecule^{-1}$ $s^{-1}$; $k_{pyrrole+NO3}$ = $4.9 \times 10^{-11}$ $cm^3$ $molecule^{-1}$ $s^{-1}$) are ∼6 orders of magnitude higher than those of "furan/pyrrole + $O_3$" ($k_{furan+O3}$ = $2.4 \times 10^{-18}$ $cm^3$ $molecule^{-1}$ $s^{-1}$; $k_{pyrrole+O3}$ = $1.6 \times 10^{-17}$ $cm^3$ $molecule^{-1}$ $s^{-1}$).[57−59] Therefore, the oxidation of pyrrole and furan in our chamber was mostly driven by $NO_3$-initiated oxidation.

The injection of the $NO_2$−$O_3$ mixture marked the start of experiments. The duration of each experiment was ∼2.2 h, during which the SOA mass concentration reached a plateau. Following this plateau, the generated SOA samples were collected on polytetrafluoroethylene membrane filters (PTFE, 46.2 mm, 2.0 $\mu$m, Tisch Scientific) for subsequent offline analysis. The collection flow rate was 20 lpm, and the collection time was 1.5 h; each filter collected the aerosols from 1.8 $m^3$ of chamber air. The experimental procedure was similar to the those reported in prior studies of high-RH


https://doi.org/10.1021/acsestair.4c00025
ACS EST Air 2024, 1, 426−437

chamber experiments.[20,21] It has been noted that the chamber wall loss of particles may be potentially different at different RHs. However, in this study, the first-order size-dependent particulate wall loss rates were comparable at both RH levels (Figure S1). Although vapor wall loss of oxidized products can be increased by higher RH, our data showed an increased trend of mass fractions of oxygenated composition in particle phase (Figure S2). Such evidence indicates that the chamber interference at higher RH did not significantly hinder the formation of highly oxidized products in SOA.[20] Experiments of each environmental condition were repeated for three times (n = 3) to confirm the reproducibility of observed phenomena and determine the uncertainties (standard deviations) of reported values.

**Particulate Size Distribution and Compositional Analysis.** The number concentration and size distribution of SOA were measured throughout the duration of the experiments by a scanning electrical mobility spectrometer (SEMS, Brechtel Manufacturing Inc.) in the diameter range of 10−800 nm with 140 bins. The bulk composition and the *in situ* molecular composition were characterized by a mini-aerosol mass spectrometer coupled with a compact time-of-flight mass spectrometer (mAMS, Aerodyne Research Inc.)[60] and an iodide-adduct time-of-flight chemical ion mass spectrometer coupled with the filter inlet for gases and aerosols system (FIGAERO-ToF-CIMS, Aerodyne Research Inc.),[61] respectively. Attenuated total reflectance Fourier-transform infrared spectrometer (ATR-FTIR, Thermo Nicolet iS50) was used to characterize the functional group fingerprints. The measured IR spectra were deconvoluted using Igor Pro 7 (WaveMetrics, Lake Oswego, OR, USA), in which the wavenumbers of identified peaks were determined. Gas chromatography−electron ionization mass spectrometry (GC/EI-MS, Agilent Technologies 6890N GC System and 5975 inert XL Mass Selective Detector) and liquid chromatography coupled with an electrospray ionization source and a quadruple-time-of-flight mass spectrometer (LC-ESI-Q-ToFMS, Agilent Technologies 1260 Infinity II and 6545 Q-ToF LC/MS) were used to analyze the molecular composition of SOA samples. Details of the instrumental setup have been published elsewhere.[40,41] Particulate effective density, organic mass fraction in aerosols, and SOA mass concentration in the chamber were calculated based on the methods described in our previous study (Table S1).[40]

The mass fractions of molecular chromophores were semi-quantified using surrogate standards analyzed by LC-ESI-Q-TOFMS or GC/EI-MS. Molecular chromophores in furan BrC were mainly carbonyls, while in pyrrole BrC accounted for both carbonyls and nitroaromatics.[15,41] Therefore, we used maleic acid ($C_4H_4O_4$), maleimide ($C_4H_3NO_2$), and nitropyrroles ($C_4H_4N_2O_2$, including 2-nitropyrrole and 3-nitropyrrole) as surrogate standards for estimating chromophores in furan BrC, carbonyl chromophores in pyrrole BrC, and nitroaromatic chromophores in pyrrole BrC, respectively. $C_4H_4O_4$ was quantified by LC-ESI-Q-TOFMS, while $C_4H_3NO_2$ and $C_4H_4N_2O_2$ were quantified by GC/EI-MS with their authentic chemical standards. The mass fractions of other molecular chromophores were estimated by eq 1.

$$MF_{chromophore} = MF_{surrogate}\frac{c_{chromophore}M_{chromophore}}{c_{surrogate}M_{surrogate}} = MF_{surrogate}R_F\frac{A_{chromophore}M_{chromophore}}{A_{surrogate}M_{surrogate}} \quad (1)$$

$MF_{chromophore}$ is the mass fraction of the characterized molecular chromophore in SOA samples; $MF_{surrogate}$ is the mass fraction of the surrogate standard in SOA samples; $c_{chromophore}$ and $c_{surrogate}$ are the molar concentrations of the characterized chromophores and the surrogate standard in the SOA samples (mol $L^{-1}$); $M_{chromophore}$ and $M_{surrogate}$ are the molar masses of the characterized chromophores and the surrogate standard in the SOA samples (g $mol^{-1}$); and $A_{chromophore}$ and $A_{surrogate}$ are the peak areas of parent ions of the characterized chromophores and the surrogate standard in their extracted ion chromatograms (EICs) measured by LC-ESI-Q-TOFMS. While the response factor ($R_F$) of molecular chromophores may exhibit certain variations compared to surrogate standards,[15] semi-quantification can still offer approximate mass fractions to elucidate their changes under different RH conditions.

**Light Absorption Properties.** The ultraviolet and visible (UV−vis) absorbance of SOA samples was measured by a UV−vis spectrophotometer (Beckman DU-640) in the range of 290−700 nm, with the reference wavelength at 700 nm. All of the SOA samples were extracted with acetonitrile (ACN), an aprotic polar solvent that is suitable for analyzing carbonyl-rich secondary BrC samples.[40] It should be noted that due to solvent selectivity, ACN may not completely extract the furan SOA and pyrrole SOA constituents from filters (i.e., extraction efficiency <100%).[15] The MAC profiles of SOA samples are calculated by eq 2.

$$MAC(\lambda) = \ln 10 \times \frac{A(\lambda) - A(700)}{b \times C_m} \quad (2)$$

$A(\lambda)$ is the wavelength ($\lambda$)-dependent absorbance, $b$ is the light path length (i.e., 1 cm), and $C_m$ is the mass concentration of SOA. Since $C_m$ was calculated by the total on-filter SOA mass (online-monitored SOA mass concentration × air volume in filter collection) over the volume of ACN solution and given the chance that some BrC components were not completely extracted with ACN, this study estimated the lower-bound limit of BrC MAC. Since SOA formation at each environmental condition was repeated three times, the average and standard deviation of MAC at each wavelength can be calculated by three replicates of SOA samples. The relative error (i.e., standard deviation over the average value) of the MAC value at each wavelength was ∼15%, as estimated by 3 repeated experiments. The wavelength dependency of $MAC(\lambda)$ was also investigated by fitting the absorption Ångström exponent (AAE), as defined by eq 3.

$$AAE = -\frac{\ln MAC(\lambda) - \ln MAC(\lambda_0)}{\ln \lambda - \ln \lambda_0} = -\frac{\ln[MAC(\lambda)/MAC(\lambda_0)]}{\ln(\lambda/\lambda_0)} \quad (3)$$

Here, $\lambda_0$ represents the reference wavelength. The fitted AAE would be equal to the slope of the linear regression of $\ln[MAC(\lambda)/MAC(\lambda_0)]$ versus $-ln(\lambda/\lambda_0)$ with a zero intercept. Since our previous studies reported that AAE can be different in the UV (290−400 nm) and visible (400−600 nm)


https://doi.org/10.1021/acsestair.4c00025
ACS EST Air 2024, 1, 426−437

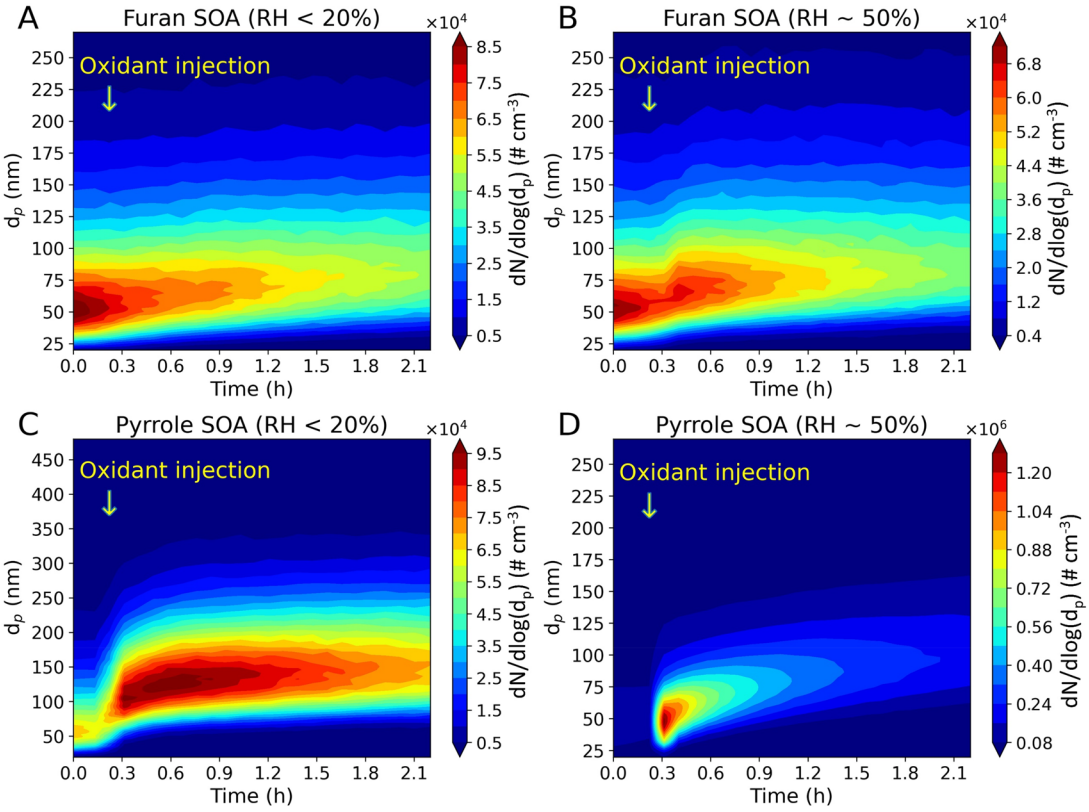


**Figure 1.** Particle size distribution dynamics of (A) furan SOA at RH <20%; (B) furan SOA at RH ~50%; (C) pyrrole SOA at RH <20%; and (D) pyrrole SOA at RH ~50%.

ranges,[14,39−41] we set $\lambda_0$ as 400 nm for fitting the AAE. However, since the AAE shown in our data can largely vary along with $\lambda$, we also derive the wavelength-dependent AAE in eq 4.

$$AAE(\lambda) = -\frac{\mathrm{d}\ln MAC(\lambda)}{\mathrm{d}\ln\lambda} = -\frac{\lambda}{MAC(\lambda)}\frac{\mathrm{d}\,MAC(\lambda)}{\mathrm{d}\lambda} \approx -\frac{\lambda}{MAC(\lambda)}\frac{MAC(\lambda+\Delta\lambda) - MAC(\lambda-\Delta\lambda)}{2\Delta\lambda} \quad (4)$$

The stepwise wavelength ($\Delta\lambda$) was set as 3 nm. $AAE(\lambda)$ was sketched by a stepwise scan to portray a more detailed wavelength dependency of MAC, while the fitted AAE values reflected the overall trend. These two representations of AAE can complementarily highlight the distinction of MAC profiles at different RH.

**Computational Methods.** Time-dependent density functional theory was employed to estimate the theoretical UV−vis spectra of molecular chromophores. All the computations were conducted using the Gaussian 16 program (revision C. 01).[62] Geometrical optimization and the computation of line-center wavelengths and oscillator strengths were performed by the B3LYP functional[63,64] with the 6-311++G(d,p) basis set,[65] as suggested in previous studies.[14,66,67] The ACN environment was simulated by the integral equation formalism extension of the polarizable continuum model.[68] The theoretical UV−Vis spectra were generated by the GaussView 6 program. The validation of our theoretical calculations was previously discussed in detail with similar BrC chromophores.[67] Cartesian coordinates for all the molecular structures are summarized in Table S2.

## RESULTS AND DISCUSSIONS

**Size Distribution Dynamics of Furan SOA and Pyrrole SOA.** Size distribution dynamics, which encompasses the change in number and size distribution of particles over time, is the physical basis of SOA formation and can be interconnected with gas-phase and/or multiphase chemistry.[69] At RH <20%, the particulate size of furan SOA gradually increased over time, but at RH ~50%, the particulate size of furan SOA rapidly increased within 10 min when furan oxidation started (Figure 1A,B). However, the particle size distribution dynamics of pyrrole SOA were different. If the response of pyrrole SOA to changes in RH is similar to that of furan SOA, then an even broader size distribution of pyrrole SOA should be observed at higher RH, because distinct growth in particulate size was observed at low RH (Figure 1C), which indicated the greater potential of pyrrole oxidation products to contribute to particles with larger size. However, at higher RH, our results unexpectedly showed a much narrower size distribution of pyrrole SOA (Figure 1D). The central diameter of the particles was still ~50 nm, comparable to that of the pre-existing particles, reflecting the limited particulate growth. Correspondingly, the particle number concentration at RH ~50% was significantly higher than that at RH <20% (Figure 1 C, D), indicating an intensive new particle formation (NPF) at RH ~50%. The rapid decrease of number concentration in Figure 1D may be attributed to the chamber wall loss and coagulation of particles. Although the intensive NPF was observed at a specific environmental condition (i.e., RH ~50% with pre-existing particles), our findings can be tightly related to wildfire smoke because RH ~50% and pre-existing particles are frequently observed in wildfire smoke.[47−49] All of these


https://doi.org/10.1021/acsestair.4c00025
ACS EST Air 2024, 1, 426−437

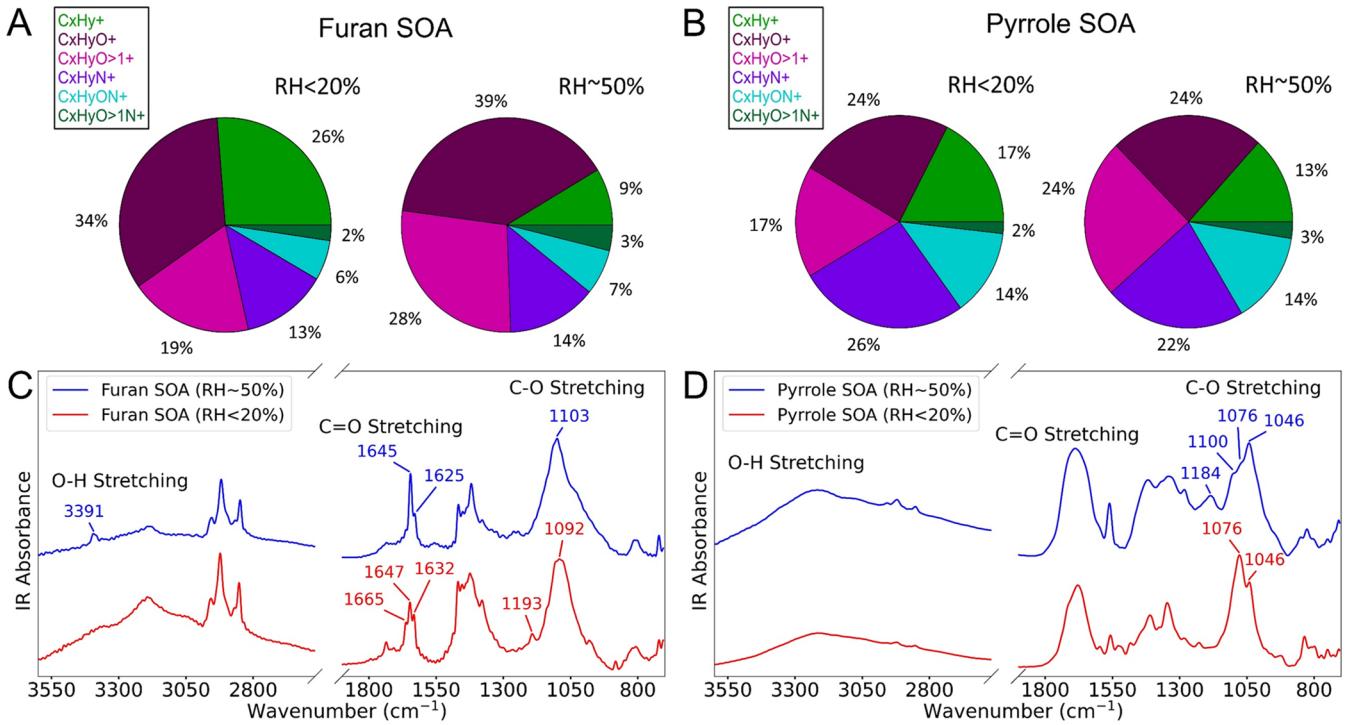


**Figure 2.** Chemical characterizations of the SOA bulk composition at RH <20% and ∼50% conditions: (A) mass fractions of compositional fragments of furan SOA; (B) mass fractions of compositional fragments of pyrrole SOA; (C) functional group fingerprints of furan SOA; and (D) functional group fingerprints of pyrrole SOA.

characteristics demonstrated the differential RH responses of furan SOA and pyrrole SOA.

The intensive NPF of pyrrole SOA was unexpectedly associated with the pre-existing particles, as revealed by our benchmark experiments. Without pre-existing particles, an increase in RH broadened the size distribution of both SOAs when oxidation started (Figure S3). The size distribution of pyrrole SOA at RH ∼50% was much broader than that at RH <20% (Figure S3C,D), indicating that higher RH boosted particle growth accompanied by NPF so that the particulate size was larger but the particulate number concentration was lower. This phenomenon reflected that higher RH without pre-existing particles was capable of facilitating the condensation of gas-phase products and the coagulation of ultrafine particles when pyrrole SOA was formed. These two processes would be promoted in the presence of pre-existing particles, which were expected to become the condensation sink.[70] However, intensive NPF was observed (Figure 1D), reflecting the boosted nucleation process regardless of the pre-existing particles. It is noted that the potential to form ultrafine particles via nucleation processes could be largely dependent on environmental conditions. The intensive NPF shown in Figure 1D suggests that the nighttime oxidation of pyrrole may have a stronger potential to induce nucleation in humid wildfire smoke. Although a thorough mechanistic elucidation may require further measurements of the critical nuclei composition, the unexpected NPF of pyrrole SOA can reflect that the nitrogen atom from the pyrrole backbone is the key to inducing a stronger potential for nucleation, as compared to furan SOA (Figure 1B,D). The "furan-pyrrole" comparisons highlighted the importance of VOC-specified physicochemical processing in wildfire-related SOA formation, which may influence the chemical composition.

**Chemical Characterization of SOA Composition.** To investigate the effects of RH on SOA composition, chemical characterization was conducted using multiple complementary instruments to determine the bulk and molecular compositions, as well as the molecular fingerprints. The bulk composition of SOA showed that higher RH increased the mass fraction of $C_xH_yO_{>1}^+$ fragments but decreased the mass fraction of $C_xH_y^+$ fragments in both SOAs (Figure 2A, B). However, at both RH conditions, the total mass fractions of nitrogen-containing fragments (i.e., $C_xH_yN^+$, $C_xH_yON^+$, and $C_xH_yO_{>1}N^+$) of either furan SOA or pyrrole SOA were roughly consistent (Figure 2A,B). It is noted that reduced nitrogen compounds (e.g., imidazole-type compounds) may be potentially generated from particle-phase reactions between organic products and the ammonium cations in the pre-existing particles.[71−75] Here, $C_2H_2N^+$, $C_2H_3N^+$, and $C_3H_3N^+$ (typical fragments of nitrogen-containing organic compounds other than organonitrates measured by mAMS[29]) were used to quantify the mass fractions of reduced nitrogen compounds (Table S3). At higher RH, the mass fraction of $C_2H_3N^+$ was higher, but the mass fractions of $C_2H_2N^+$ and $C_3H_3N^+$ were lower. However, the total mass fraction of these fragments was roughly constant at both RHs, indicating that the change in RH had a minor influence on the formation of reduced nitrogen. All these results indicated that the compositional change at higher RH mainly accounted for the generation of oxygenated products.

Moreover, our ATR-FTIR measurements showed the difference in oxygenated functional group fingerprints at different RH, including the hydroxyl group (O−H) stretching, the carbon−oxygen double bond (C═O) stretching, and the carbon−oxygen−carbon (C−O−C) stretching (Figure 2). Functional groups were assigned to the wavenumbers based on previous IR studies of SOA composition.[76] In furan SOA,


https://doi.org/10.1021/acsestair.4c00025
ACS EST Air 2024, 1, 426−437

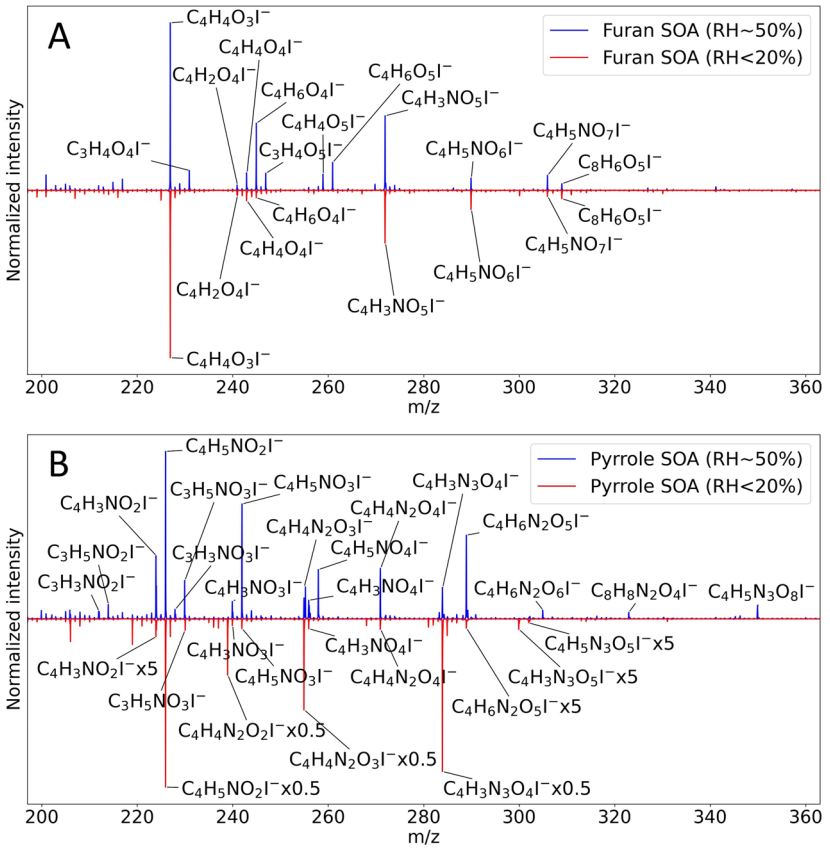


**Figure 3.** Molecular characterization of oxygenated products in (A) furan SOA and (B) pyrrole SOA at RH <20% and ~50% conditions.

the wavenumber of the C−O peak shifted while both the number and wavenumbers of C═O peaks changed. A new O−H peak at 3391 $cm^{-1}$ was observed, but the C−O peak at 1193 $cm^{-1}$ disappeared at higher RH (Figure 2C). These results indicated that the change in RH may greatly alter the oxygenated constituents in furan SOA. While in pyrrole SOA, O−H and C═O peaks were similar at both RH, while at higher RH two new C−O−C peaks (1100 $cm^{-1}$ and 1184 $cm^{-1}$) were identified (Figure 2D). Since the C−O−C structure cannot be inherited from the pyrrole backbone, the new C−O−C peaks may be attributed to RH-modulated gas-phase and/or multiphase oxidation on pyrrole SOA. The observed results of functional group fingerprints from SOA formed at different RH levels reflected that higher RH could cause a shift in the distribution of wavenumbers of oxygenated functional groups suggesting a considerable change in the chemical composition of oxygenated compounds with RH.

The effect of RH on the oxygenated products was further investigated through the molecular characterization of SOA samples. The average of the hydrogen-to-carbon (H/C) and the oxygen-to-carbon (O/C) ratios (i.e., ⟨H/C⟩ and ⟨O/C⟩), weighted by intensity from FIGAERO-ToF-CIMS measurements, of both SOA constituents increased with higher RH (Table S4). This suggests that higher RH levels can enhance the saturation and oxygenation levels of SOA constituents (Figure 3). The increasing ⟨H/C⟩ ratio decreased the intensity-weighted average of double bond equivalence (DBE) (i.e., ⟨DBE⟩) (Figure 3). However, the nitrogen-to-carbon (N/C) ratio (i.e., ⟨N/C⟩) decreased at higher RH in pyrrole SOA constituents while kept constant in furan SOA constituents (Table S4), indicating that the formation of nitrogen-containing products in pyrrole SOA characterized by FIGAERO-ToF-CIMS were more sensitive to RH change. In furan SOA, the highest peaks at both RH conditions were attributed to $C_4H_4O_3$, while the presence of its oxygenated products $C_4H_4O_4$ and $C_4H_4O_5$ was also observed (Figure 3A). It should be noted that $C_4H_4O_5$ was only observed at higher RH, which may account for the enhanced oxygenation of furan SOA constituents. In pyrrole SOA, the formation of new oxygenated products with higher H/C and O/C ratios (e.g., $C_4H_6N_2O_6$, $C_4H_5N_3O_8$) was observed (Figure 3B). The peak intensity ratios of $C_4H_5NO_3$ to $C_4H_5NO_2$ increased significantly at higher RH, contributing to the higher oxygenation level of pyrrole SOA constituents at higher RH. All of these findings not only confirmed the formation of oxygenated products at higher RH, but also demonstrated a higher saturation level of SOA constituents. The increased saturation and oxygenation levels at higher RH could be attributed to multiple processes, such as gas-phase chemistry, reactive uptake of radicals, aerosol-phase reactions, etc.[16−27] Because multiple physicochemical processes interplay during SOA formation, further research is necessary to provide a more comprehensive understanding of the influence of each individual process involved. The compositional change due to these processes may further affect the secondary BrC light absorption properties.

**Light Absorption Properties of Secondary BrC.** The light absorption properties of secondary BrC can be affected by SOA compositional changes. Our results showed that higher RH significantly reduced the MAC profiles for both SOAs, wherein both SOAs can fall in the moderately absorptive BrC category at RH <20% and the weakly absorptive BrC category


https://doi.org/10.1021/acsestair.4c00025
ACS EST Air 2024, 1, 426−437

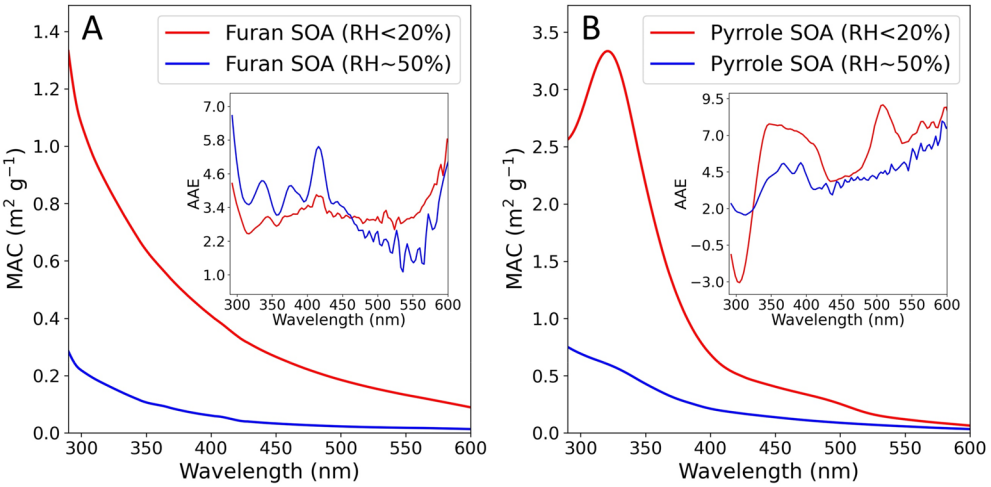


**Figure 4.** MAC profiles of (A) furan BrC and (B) pyrrole BrC at both RH <20% and ~50% conditions. The inset panels show the AAE changes along with wavelengths.

at RH ~50% (Figure 4).[77] As compared with SOA derived from other precursors under various oxidation conditions, furan SOA was moderately absorbing at RH <20% and least absorbing at RH ~50%, while pyrrole SOA was highly absorbing at RH <20% and less absorbing at RH ~50% (Table S5).[28,30,50,78] These comparisons indicated that the effects of RH on light absorption can be sensitive to SOA precursors and their explicit chemical formation pathways.

The reduction in MAC profiles at higher RH cannot be not attributed to the aqueous chemistry between ammonium cations and SOA constituents,[72,79,80] as these reactions may actually enhance the MAC (Text S1; Figures S4 and S5). Instead, the reduced MAC observed at higher RH may be linked to enhanced formation of oxygenated products. Our results showed that non-absorbing oxygenated compounds (i.e., those with DBE = 0) were detected only at RH ~50% (Figure S6). Some of the non-absorbing compounds were the major constituents in SOA samples (Figure S7). These molecules have higher molecular weights and possess at least 8 carbons and 10 oxygens. Such high level of oxygenation only observed at higher RH suggested that higher RH may reduce MAC mostly via enhancing gas-phase and/or multiphase oxidation of SOA constituents.

As illustrated by the AAE curves in the inset panels shown in Figure 4, the compositional change of BrC chromophores was also reflected in the changed shape of MAC profiles. At both RH conditions, the AAE curves of furan BrC were comparable, even though higher RH slightly increased the AAE in the UV range but slightly decreased in the visible range (Figure 4A). The fitted AAE showed comparable values at RH <20% and ~50% in both UV and visible ranges (Table 1). However, the AAE curves of pyrrole BrC exhibited significant differences at RH <20% and ~50%; a twisting curve was shown at RH <20%, whereas a monotonously increased trend with a small bend was shown at RH ~50% (Figure 4B). The fitted AAE values were smaller at RH ~50% (Table 1), indicating that the overall wavelength dependency of MAC profiles of pyrrole BrC was diminished by higher RH levels. Taken together, the reduced MAC profiles with altered wavelength dependency point to a change in the composition of BrC chromophores.

**Table 1. Fitted AAE and $R^2$ in the Linear Regression of MAC in the UV (290−400 nm) and Visible (400−600 nm) Ranges**

| | | AAE | | $R^2$ | |
|---|---|---|---|---|---|
| BrC Samples | RH | UV | Visible | UV | Visible |
| Furan BrC | <20% | 3.00 | 3.21 | 1.00 | 1.00 |
| | ~50% | 3.86 | 3.18 | 1.00 | 0.99 |
| Pyrrole BrC | <20% | 5.74 | 5.79 | 0.95 | 0.99 |
| | ~50% | 3.88 | 4.07 | 0.99 | 1.00 |

**Mass Fractions of BrC Chromophores in SOA.** The mass fractions of molecular chromophores observed at both RH can aid in understanding the effect of RH on the MAC profiles. Semi-quantification was performed for molecular chromophores characterized in this study (Table S6). Most of the characterized chromophores listed in Table S6 were also reported in our previous studies of furan- and pyrrole-derived secondary BrC.[14,15,39−41] While the mass fractions of some less abundant chromophores (e.g., $C_4H_3NO_3$) were similar at both RH, most of the characterized chromophores showed lower mass fractions at higher RH. In Figure 5, two newly identified compounds ($C_8H_5NO_6$ and $C_4H_2N_4O_6$) are presented as examples for detailed discussions. $C_8H_5NO_6$ was characterized as 3-nitrophthalic acid (Figure S8A,C), whereas $C_4H_2N_4O_6$ showed two peaks (Figure 5B), which corresponded to 5,6-dinitro-4*H*-1,2,4-oxadiazine-3-carbaldehyde (Figure S8B,D) and 2,3,4-trinitro-pyrrole (Figure S9). At higher RH, the mass-normalized intensity in their extracted ion chromatograms (EICs) nearly disappeared (Figure 5). Since molecular chromophores have different contributions to the MAC profiles at different wavelengths,[15] their decreased mass fractions can reduce the MAC in specific wavelength regions. Because the spectral absorption of 3-nitrophthalic acid only covers the UV range (Figure 5A), it contributes to the reduction of MAC of furan BrC in the UV range. The reduction of MAC in the visible range may be attributed to the decreased mass fractions of other chromophores whose spectra can extend to above 400 nm (e.g., $C_4H_2O_4$).[15] The spectral absorption of 5,6-dinitro-4H-1,2,4-oxadiazine-3-carbaldehyde covers both UV and visible ranges (Figure 5B), with a spectral shape similar to the MAC profile of pyrrole BrC at low RH (Figure 4B). More chromophores, such as 2,3,4-trinitro-pyrrole (Figure S9A) and dinitro-pyrroles ($C_4H_3N_3O_4$),[41] can also contribute to the MAC profiles in the UV range.


https://doi.org/10.1021/acsestair.4c00025
ACS EST Air 2024, 1, 426−437

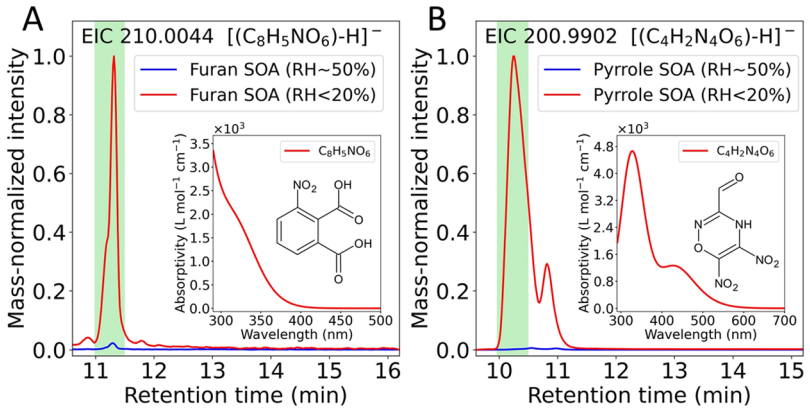


**Figure 5.** Characterization of molecular chromophores at RH <20% and ~50% conditions: (A) $C_8H_5NO_6$ in furan SOA; (B) $C_4H_2N_4O_6$ in pyrrole SOA. The mass-normalized intensity was calculated by the EIC intensity over the estimated mass of SOA samples, with the maximum value in each panel scaled to 1.0. The inset panels show the theoretical UV−vis spectra of molecular chromophores.

While it is possible that higher RH may potentially facilitate the production of new molecular chromophores with a red shift of light absorption towards longer wavelengths,[30] our findings revealed that the decrease in mass fractions of various molecular chromophores was mostly responsible for the altered wavelength dependency and lowered profiles of the MAC. The evidence together demonstrates the important role of molecular chromophores in bridging the change in environmental conditions to the light absorption properties of secondary BrC.

## ■ ATMOSPHERIC IMPLICATIONS

This study provides evidence for the role of RH in modulating secondary BrC formation from heterocyclic VOCs, a significant group of SOA precursors in wildfire smoke,[34] through changes in size distribution dynamics, chemical composition, and light absorption properties. We also highlight the necessity of understanding explicit physicochemical pathways for evaluating the effects of RH on the climate impacts of wildfire smoke aerosols because multiple physicochemical processes can interplay during SOA formation, which can in turn alter the secondary BrC chemical composition and light absorption properties. The observations presented in this study demonstrate the intercorrelation of aerosol size distribution, chemical composition, and light absorption properties. Specifically, the increased saturation and oxygenation levels of SOA composition at higher RH may promote the formation of non-absorbing oxygenated compounds, which can lead to decreased MAC profiles. Such process-level knowledge can aid in better understanding the effects of RH on BrC light absorption in wildfire smoke.

In contrast to secondary BrC derived from homocyclic VOCs (e.g., toluene), in which the production of nitroaromatic chromophores can be enhanced by higher RH,[28,81,82] our findings indicate that higher RH can lead to decreased mass fractions of nitrogen-containing chromophores (e.g., $C_8H_5NO_6$ and $C_4H_2N_4O_6$) in furan- and pyrrole-derived BrC. Such a difference highlights the critical role of SOA precursors and the molecular characteristics of chromophores in the effects of RH on secondary BrC formation. It should be noted that RH may exhibit a more complicated influence on secondary BrC light absorption (e.g., the non-monotonic RH dependency of MAC[50,82]) or have less significant effects if the nitrogen content of secondary BrC is limited.[82] Given this complexity, understanding the explicit physicochemical processes of SOA formation would be the key to regulating secondary BrC formation. Our findings reveal that RH can greatly modulate the explicit physicochemical processing of secondary BrC formation and further alter the BrC-related radiative impacts of wildfire smoke. Therefore, this study highlights the importance of considering RH as a critical environmental factor in more accurate assessments of the climate effects of wildfire smoke aerosols.

Furthermore, this study can serve as a benchmark to help understand how the complex atmospheric environment affects the climate impacts of smoke aerosols at the process level. Our findings reveal that dry conditions can lead to strongly absorbing secondary BrC derived from the nighttime oxidation of heterocyclic VOCs. This route may partially contribute to the strong BrC light absorption in dry wildfire smoke, as evident from recent field studies.[12,83] More importantly, the reduced light absorption and the enhanced oxygenated mass were not only found in the $NO_3$-driven secondary BrC formation, but also in the aging processes of biomass-burning aerosols.[84,85] This common characteristic suggests that the processing-level understanding reported in this study may be partially applicable to a wider range of physicochemical processes related to wildfire smoke. In addition, while previous studies have highlighted the importance of low-volatility high-molecular-weight (≥400 Da) chromophores in optical properties of primary combustion BrC,[77,86−88] this study and our prior work of furan SOA and pyrrole SOA suggest that nighttime oxidation of heterocyclic VOCs may mainly contribute to BrC chromophores with low molecular weight (<400 Da) in wildfire smoke aerosols.[14,15,39−41] Further research is needed to incorporate our findings into climate models to better estimate the RH influence on the radiative effects of wildfire smoke. Overall, our study demonstrates that environmental conditions such as RH in wildfire smoke can modulate secondary BrC formation and hence regulate the radiative impacts of unabated wildfires in the context of climate change.

## ■ ASSOCIATED CONTENT

### Supporting Information

The Supporting Information is available free of charge at https://pubs.acs.org/doi/10.1021/acsestair.4c00025.



https://doi.org/10.1021/acsestair.4c00025
ACS EST Air 2024, 1, 426−437

Details about the supplementary experiments; Cartesian coordinates for geometrical structures of molecular chromophores in the TD-DFT calculations; summary of particulate effective density, organic mass fraction, and mass concentration of generated SOA; mass fractions of the imidazole-type fragments in SOA; intensity-weighted average and standard deviation of H/C, O/C, and N/C ratios and DBE of SOA composition characterized by FIGAERO-ToF-CIMS; $MAC_{365}$ from this study and prior studies of secondary BrC; mass fractions of molecular chromophores in SOA; first-order wall loss rate constants at both RH; time series of $C_xH_yO_{>1}^+$ and $C_xH_y^+$; SOA size distribution dynamics without pre-existing particles; MAC profiles in the solution experiments; characterized products from aqueous-phase chemistry; extracted ion chromatograms of non-absorbing oxygenated compounds; base peak chromatograms of SOA samples and selected non-absorbing oxygenated compounds; characterization of 3-nitrophthalic acid and 5,6-dinitro-4H-1,2,4-oxadiazine-3-carbaldehyde; and characterization of 2,3,4-trinitropyrrole (PDF)

## AUTHOR INFORMATION


### Corresponding Author

**Ying-Hsuan Lin** − *Department of Environmental Sciences, University of California, Riverside, California 92521, United States;* orcid.org/0000-0001-8904-1287; Phone: +1-951-827-3785; Email: ying-hsuan.lin@ucr.edu

### Authors

**Kunpeng Chen** − *Department of Environmental Sciences, University of California, Riverside, California 92521, United States;* orcid.org/0000-0002-9430-9257

**Caitlin Hamilton** − *Department of Chemistry, University of California, Riverside, California 92521, United States*

**Bradley Ries** − *Department of Environmental Sciences, University of California, Riverside, California 92521, United States*

**Michael Lum** − *Department of Environmental Sciences, University of California, Riverside, California 92521, United States*

**Raphael Mayorga** − *Department of Chemistry, University of California, Riverside, California 92521, United States*

**Linhui Tian** − *Department of Environmental Sciences, University of California, Riverside, California 92521, United States;* orcid.org/0009-0009-2147-1518

**Roya Bahreini** − *Department of Environmental Sciences, University of California, Riverside, California 92521, United States;* orcid.org/0000-0001-8292-5338

**Haofei Zhang** − *Department of Chemistry, University of California, Riverside, California 92521, United States;* orcid.org/0000-0002-7936-4493

Complete contact information is available at: https://pubs.acs.org/10.1021/acsestair.4c00025


### Notes

The authors declare no competing financial interest.

## ACKNOWLEDGMENTS

This work was supported by NSF AGS-1953905 and the UCR Hellman Fellowship granted to Ying-Hsuan Lin. Michael Lum was supported by an NSF graduate research fellowship. We thank Dr. Jie Zhou and Dr. Lingchao Zhu at UCR Analytical Chemistry Instrumentation Facility (ACIF) for their assistance with UPLC-ESI-Q-TOFMS (supported by NSF CHE-0541848) and Thermo Nicolet 6700 ATR-FTIR (supported by UCR Chemistry ACIF Fund).

## REFERENCES


(1) Ferrero, L.; Močnik, G.; Cogliati, S.; Gregorič, A.; Colombo, R.; Bolzacchini, E. Heating Rate of Light Absorbing Aerosols: Time-Resolved Measurements, the Role of Clouds, and Source Identification. *Environ. Sci. Technol.* **2018**, *52* (6), 3546−3555.

(2) Liu, D.; He, C.; Schwarz, J. P.; Wang, X. Lifecycle of light-absorbing carbonaceous aerosols in the atmosphere. *npj Clim. Atmos. Sci.* **2020**, *3* (1), 40.

(3) Ding, K.; Huang, X.; Ding, A.; Wang, M.; Su, H.; Kerminen, V.-M.; Petäjä, T.; Tan, Z.; Wang, Z.; Zhou, D.; Sun, J.; Liao, H.; Wang, H.; Carslaw, K.; Wood, R.; Zuidema, P.; Rosenfeld, D.; Kulmala, M.; Fu, C.; Pöschl, U.; Cheng, Y.; Andreae, M. O. Aerosol-boundary-layer-monsoon interactions amplify semi-direct effect of biomass smoke on low cloud formation in Southeast Asia. *Nat. Commun.* **2021**, *12* (1), 6416.

(4) Bowman, D. M. J. S.; Balch, J. K.; Artaxo, P.; Bond, W. J.; Carlson, J. M.; Cochrane, M. A.; D'Antonio, C. M.; DeFries, R. S.; Doyle, J. C.; Harrison, S. P.; Johnston, F. H.; Keeley, J. E.; Krawchuk, M. A.; Kull, C. A.; Marston, J. B.; Moritz, M. A.; Prentice, I. C.; Roos, C. I.; Scott, A. C.; Swetnam, T. W.; van der Werf, G. R.; Pyne, S. J. Fire in the Earth System. *Science* **2009**, *324* (5926), 481−484.

(5) Jolly, W. M.; Cochrane, M. A.; Freeborn, P. H.; Holden, Z. A.; Brown, T. J.; Williamson, G. J.; Bowman, D. M. J. S. Climate-induced variations in global wildfire danger from 1979 to 2013. *Nat. Commun.* **2015**, *6* (1), 7537.

(6) Goss, M.; Swain, D. L.; Abatzoglou, J. T.; Sarhadi, A.; Kolden, C. A.; Williams, A. P.; Diffenbaugh, N. S. Climate change is increasing the likelihood of extreme autumn wildfire conditions across California. *Environ. Res. Lett.* **2020**, *15* (9), No. 094016.

(7) Andreae, M. O.; Merlet, P. Emission of trace gases and aerosols from biomass burning. *Global Biogeochemical Cycles* **2001**, *15* (4), 955−966.

(8) Andreae, M. O. Emission of trace gases and aerosols from biomass burning − an updated assessment. *Atmos. Chem. Phys.* **2019**, *19* (13), 8523−8546.

(9) Szopa, S.; Naik, V.; Adhikary, B.; Artaxo, P.; Berntsen, T.; Collins, W. D.; Fuzzi, S.; Gallardo, L.; Kiendler-Scharr, A.; Klimont, Z.; Liao, H.; Unger, N.; Zanis, P. *Short-Lived Climate Forcers. In Climate Change 2021: The Physical Science Basis. Contribution of Working Group I to the Sixth Assessment Report of the Intergovernmental Panel on Climate Change* Masson-Delmotte, V., Zhai, P., Pirani, A., Connors, S. L., Péan, C., Berger, S., Caud, N., Chen, Y., Goldfarb, L., Gomis, M.I., Huang, M., Leitzell, K., Lonnoy, E., Matthews, J.B.R., Maycock, T.K., Waterfield, T., Yelekçi, O., Yu, R., Zhou, B., Eds.; Cambridge University Press: Cambridge, United Kingdom, and New York, NY, USA, 2021; pp 817−922.

(10) Bond, T. C.; Streets, D. G.; Yarber, K. F.; Nelson, S. M.; Woo, J.-H.; Klimont, Z. A technology-based global inventory of black and organic carbon emissions from combustion. *J. Geophys. Res. Atmos.* **2004**, *109*, No. D14203.

(11) Yu, P.; Toon, O. B.; Bardeen, C. G.; Zhu, Y.; Rosenlof, K. H.; Portmann, R. W.; Thornberry, T. D.; Gao, R.-S.; Davis, S. M.; Wolf, E. T.; de Gouw, J.; Peterson, D. A.; Fromm, M. D.; Robock, A. Black carbon lofts wildfire smoke high into the stratosphere to form a persistent plume. *Science* **2019**, *365* (6453), 587−590.

(12) Chakrabarty, R. K.; Shetty, N. J.; Thind, A. S.; Beeler, P.; Sumlin, B. J.; Zhang, C.; Liu, P.; Idrobo, J. C.; Adachi, K.; Wagner, N. L.; Schwarz, J. P.; Ahern, A.; Sedlacek, A. J.; Lambe, A.; Daube, C.; Lyu, M.; Liu, C.; Herndon, S.; Onasch, T. B.; Mishra, R. Shortwave absorption by wildfire smoke dominated by dark brown carbon. *Nat. Geosci.* **2023**, *16* (8), 683−688.

(13) Akherati, A.; He, Y.; Garofalo, L. A.; Hodshire, A. L.; Farmer, D. K.; Kreidenweis, S. M.; Permar, W.; Hu, L.; Fischer, E. V.; Jen, C. N.; Goldstein, A. H.; Levin, E. J. T.; DeMott, P. J.; Campos, T. L.; Flocke, F.; Reeves, J. M.; Toohey, D. W.; Pierce, J. R.; Jathar, S. H. Dilution and photooxidation driven processes explain the evolution of organic aerosol in wildfire plumes. *Environ. Sci. Atmos.* **2022**, *2* (5), 1000−1022.
(14) Chen, K.; Mayorga, R.; Raeofy, N.; Lum, M.; Woods, M.; Bahreini, R.; Zhang, H.; Lin, Y.-H. Effects of Nitrate Radical Levels and Pre-Existing Particles on Secondary Brown Carbon Formation from Nighttime Oxidation of Furan. *ACS Earth Space Chem.* **2022**, *6* (11), 2709−2721.
(15) Chen, K.; Mayorga, R.; Hamilton, C.; Bahreini, R.; Zhang, H.; Lin, Y.-H. Contribution of Carbonyl Chromophores in Secondary Brown Carbon from Nighttime Oxidation of Unsaturated Heterocyclic Volatile Organic Compounds. *Environ. Sci. Technol.* **2023**, *57* (48), 20085−20096.
(16) Seinfeld, J. H.; Erdakos, G. B.; Asher, W. E.; Pankow, J. F. Modeling the Formation of Secondary Organic Aerosol (SOA). 2. The Predicted Effects of Relative Humidity on Aerosol Formation in the α-Pinene-, β-Pinene-, Sabinene-, Δ3-Carene-, and Cyclohexene-Ozone Systems. *Environ. Sci. Technol.* **2001**, *35* (9), 1806−1817.
(17) Jonsson, Å. M.; Hallquist, M.; Ljungström, E. Impact of Humidity on the Ozone Initiated Oxidation of Limonene, Δ3-Carene, and α-Pinene. *Environ. Sci. Technol.* **2006**, *40* (1), 188−194.
(18) Nguyen, T. B.; Roach, P. J.; Laskin, J.; Laskin, A.; Nizkorodov, S. A. Effect of humidity on the composition of isoprene photooxidation secondary organic aerosol. *Atmos. Chem. Phys.* **2011**, *11* (14), 6931−6944.
(19) Saukko, E.; Lambe, A. T.; Massoli, P.; Koop, T.; Wright, J. P.; Croasdale, D. R.; Pedernera, D. A.; Onasch, T. B.; Laaksonen, A.; Davidovits, P.; Worsnop, D. R.; Virtanen, A. Humidity-dependent phase state of SOA particles from biogenic and anthropogenic precursors. *Atmos. Chem. Phys.* **2012**, *12* (16), 7517−7529.
(20) Boyd, C. M.; Sanchez, J.; Xu, L.; Eugene, A. J.; Nah, T.; Tuet, W. Y.; Guzman, M. I.; Ng, N. L. Secondary organic aerosol formation from the β-pinene+NO3 system: effect of humidity and peroxy radical fate. *Atmos. Chem. Phys.* **2015**, *15* (13), 7497−7522.
(21) Boyd, C. M.; Nah, T.; Xu, L.; Berkemeier, T.; Ng, N. L. Secondary Organic Aerosol (SOA) from Nitrate Radical Oxidation of Monoterpenes: Effects of Temperature, Dilution, and Humidity on Aerosol Formation, Mixing, and Evaporation. *Environ. Sci. Technol.* **2017**, *51* (14), 7831−7841.
(22) Stirnweis, L.; Marcolli, C.; Dommen, J.; Barmet, P.; Frege, C.; Platt, S. M.; Bruns, E. A.; Krapf, M.; Slowik, J. G.; Wolf, R.; Prévôt, A. S. H.; Baltensperger, U.; El-Haddad, I. Assessing the influence of NOx concentrations and relative humidity on secondary organic aerosol yields from α-pinene photo-oxidation through smog chamber experiments and modelling calculations. *Atmos. Chem. Phys.* **2017**, *17* (8), 5035−5061.
(23) Liu, S.; Tsona, N. T.; Zhang, Q.; Jia, L.; Xu, Y.; Du, L. Influence of relative humidity on cyclohexene SOA formation from OH photooxidation. *Chemosphere* **2019**, *231*, 478−486.
(24) Petters, S. S.; Kreidenweis, S. M.; Grieshop, A. P.; Ziemann, P. J.; Petters, M. D. Temperature- and Humidity-Dependent Phase States of Secondary Organic Aerosols. *Geophys. Res. Lett.* **2019**, *46* (2), 1005−1013.
(25) Chen, T.; Chu, B.; Ma, Q.; Zhang, P.; Liu, J.; He, H. Effect of relative humidity on SOA formation from aromatic hydrocarbons: Implications from the evolution of gas- and particle-phase species. *Sci. Total Environ.* **2021**, *773*, No. 145015.
(26) Wang, Y.; Voliotis, A.; Shao, Y.; Zong, T.; Meng, X.; Du, M.; Hu, D.; Chen, Y.; Wu, Z.; Alfarra, M. R.; McFiggans, G. Phase state of secondary organic aerosol in chamber photo-oxidation of mixed precursors. *Atmos. Chem. Phys.* **2021**, *21* (14), 11303−11316.
(27) Liu, S.; Wang, Y.; Xu, X.; Wang, G. Effects of NO2 and RH on secondary organic aerosol formation and light absorption from OH oxidation of *o*-xylene. *Chemosphere* **2022**, *308*, No. 136541.
(28) Liu, J.; Lin, P.; Laskin, A.; Laskin, J.; Kathmann, S. M.; Wise, M.; Caylor, R.; Imholt, F.; Selimovic, V.; Shilling, J. E. Optical properties and aging of light-absorbing secondary organic aerosol. *Atmos. Chem. Phys.* **2016**, *16* (19), 12815−12827.
(29) Cui, Y.; Frie, A. L.; Dingle, J. H.; Zimmerman, S.; Frausto-Vicencio, I.; Hopkins, F.; Bahreini, R. Influence of Ammonia and Relative Humidity on the Formation and Composition of Secondary Brown Carbon from Oxidation of 1-Methylnaphthalene and Longifolene. *ACS Earth Space Chem.* **2021**, *5* (4), 858−869.
(30) Klodt, A. L.; Aiona, P. K.; MacMillan, A. C.; Ji Lee, H.; Zhang, X.; Helgestad, T.; Novak, G. A.; Lin, P.; Laskin, J.; Laskin, A.; Bertram, T. H.; Cappa, C. D.; Nizkorodov, S. A. Effect of relative humidity, NOx, and ammonia on the physical properties of naphthalene secondary organic aerosols. *Environ. Sci. Atmos.* **2023**, *3* (6), 991−1007.
(31) Song, C.; Gyawali, M.; Zaveri, R. A.; Shilling, J. E.; Arnott, W. P. Light absorption by secondary organic aerosol from α-pinene: Effects of oxidants, seed aerosol acidity, and relative humidity. *J. Geophys. Res. Atmos.* **2013**, *118* (20), 11,741−11,749.
(32) Sullivan, A. P.; Pokhrel, R. P.; Shen, Y.; Murphy, S. M.; Toohey, D. W.; Campos, T.; Lindaas, J.; Fischer, E. V.; Collett, J. L., Jr Examination of brown carbon absorption from wildfires in the western US during the WE-CAN study. *Atmos. Chem. Phys.* **2022**, *22* (20), 13389−13406.
(33) Gupta, R. R.; Kumar, M.; Gupta, V. Five-Membered Heterocycles with One Heteroatom. In *Heterocyclic Chemistry: Vol. II: Five-Membered Heterocycles*; Gupta, R. R., Kumar, M., Gupta, V., Eds.; Springer Berlin Heidelberg: Berlin, Heidelberg, 1999; pp 3−179.
(34) Palm, B. B.; Peng, Q.; Fredrickson, C. D.; Lee, B. H.; Garofalo, L. A.; Pothier, M. A.; Kreidenweis, S. M.; Farmer, D. K.; Pokhrel, R. P.; Shen, Y.; Murphy, S. M.; Permar, W.; Hu, L.; Campos, T. L.; Hall, S. R.; Ullmann, K.; Zhang, X.; Flocke, F.; Fischer, E. V.; Thornton, J. A. Quantification of organic aerosol and brown carbon evolution in fresh wildfire plumes. *Proc. Natl. Acad. Sci. U.S.A.* **2020**, *117* (47), 29469.
(35) Hatch, L. E.; Luo, W.; Pankow, J. F.; Yokelson, R. J.; Stockwell, C. E.; Barsanti, K. C. Identification and quantification of gaseous organic compounds emitted from biomass burning using two-dimensional gas chromatography−time-of-flight mass spectrometry. *Atmos. Chem. Phys.* **2015**, *15* (4), 1865−1899.
(36) Koss, A. R.; Sekimoto, K.; Gilman, J. B.; Selimovic, V.; Coggon, M. M.; Zarzana, K. J.; Yuan, B.; Lerner, B. M.; Brown, S. S.; Jimenez, J. L.; Krechmer, J.; Roberts, J. M.; Warneke, C.; Yokelson, R. J.; de Gouw, J. Non-methane organic gas emissions from biomass burning: identification, quantification, and emission factors from PTR-ToF during the FIREX 2016 laboratory experiment. *Atmos. Chem. Phys.* **2018**, *18* (5), 3299−3319.
(37) Permar, W.; Wang, Q.; Selimovic, V.; Wielgasz, C.; Yokelson, R. J.; Hornbrook, R. S.; Hills, A. J.; Apel, E. C.; Ku, I. T.; Zhou, Y.; Sive, B. C.; Sullivan, A. P.; Collett, J. L., Jr; Campos, T. L.; Palm, B. B.; Peng, Q.; Thornton, J. A.; Garofalo, L. A.; Farmer, D. K.; Kreidenweis, S. M.; Levin, E. J. T.; DeMott, P. J.; Flocke, F.; Fischer, E. V.; Hu, L. Emissions of Trace Organic Gases From Western U.S. Wildfires Based on WE-CAN Aircraft Measurements. *J. Geophys. Res. Atmos.* **2021**, *126* (11), No. e2020JD033838.
(38) Decker, Z. C. J.; Zarzana, K. J.; Coggon, M.; Min, K.-E.; Pollack, I.; Ryerson, T. B.; Peischl, J.; Edwards, P.; Dubé, W. P.; Markovic, M. Z.; Roberts, J. M.; Veres, P. R.; Graus, M.; Warneke, C.; de Gouw, J.; Hatch, L. E.; Barsanti, K. C.; Brown, S. S. Nighttime Chemical Transformation in Biomass Burning Plumes: A Box Model Analysis Initialized with Aircraft Observations. *Environ. Sci. Technol.* **2019**, *53* (5), 2529−2538.
(39) Jiang, H.; Frie, A. L.; Lavi, A.; Chen, J. Y.; Zhang, H.; Bahreini, R.; Lin, Y.-H. Brown Carbon Formation from Nighttime Chemistry of Unsaturated Heterocyclic Volatile Organic Compounds. *Environ. Sci. Technol. Lett.* **2019**, *6* (3), 184−190.
(40) Chen, K.; Raeofy, N.; Lum, M.; Mayorga, R.; Woods, M.; Bahreini, R.; Zhang, H.; Lin, Y.-H. Solvent effects on chemical

composition and optical properties of extracted secondary brown carbon constituents. *Aerosol Sci. Technol.* **2022**, *56* (10), 917−930.
(41) Mayorga, R.; Chen, K.; Raeofy, N.; Woods, M.; Lum, M.; Zhao, Z.; Zhang, W.; Bahreini, R.; Lin, Y.-H.; Zhang, H. Chemical Structure Regulates the Formation of Secondary Organic Aerosol and Brown Carbon in Nitrate Radical Oxidation of Pyrroles and Methylpyrroles. *Environ. Sci. Technol.* **2022**, *56* (12), 7761−7770.
(42) Akagi, S. K.; Craven, J. S.; Taylor, J. W.; McMeeking, G. R.; Yokelson, R. J.; Burling, I. R.; Urbanski, S. P.; Wold, C. E.; Seinfeld, J. H.; Coe, H.; Alvarado, M. J.; Weise, D. R. Evolution of trace gases and particles emitted by a chaparral fire in California. *Atmos. Chem. Phys.* **2012**, *12* (3), 1397−1421.
(43) Westerling, A. L.; Gershunov, A.; Brown, T. J.; Cayan, D. R.; Dettinger, M. D. Climate and Wildfire in the Western United States. *Bull. Am. Meteor. Soc.* **2003**, *84* (5), 595−604.
(44) Holden, Z. A.; Swanson, A.; Luce, C. H.; Jolly, W. M.; Maneta, M.; Oyler, J. W.; Warren, D. A.; Parsons, R.; Affleck, D. Decreasing fire season precipitation increased recent western US forest wildfire activity. *Proc. Natl. Acad. Sci. U.S.A.* **2018**, *115* (36), E8349−E8357.
(45) Jiang, Y.; Zhou, L.; Raghavendra, A. Observed changes in fire patterns and possible drivers over Central Africa. *Environ. Res. Lett.* **2020**, *15* (9), No. 0940b8.
(46) Ramo, R.; Roteta, E.; Bistinas, I.; van Wees, D.; Bastarrika, A.; Chuvieco, E.; van der Werf, G. R. African burned area and fire carbon emissions are strongly impacted by small fires undetected by coarse resolution satellite data. *Proc. Natl. Acad. Sci. U.S.A.* **2021**, *118* (9), No. e2011160118.
(47) Hobbs, P. V.; Sinha, P.; Yokelson, R. J.; Christian, T. J.; Blake, D. R.; Gao, S.; Kirchstetter, T. W.; Novakov, T.; Pilewskie, P. Evolution of gases and particles from a savanna fire in South Africa. *J. Geophys. Res. Atmos.* **2003**, *108* (D13), 8485.
(48) Junghenn Noyes, K.; Kahn, R.; Sedlacek, A.; Kleinman, L.; Limbacher, J.; Li, Z. Wildfire Smoke Particle Properties and Evolution, from Space-Based Multi-Angle Imaging. *Remote Sens.* **2020**, *12* (5), 769.
(49) Huang, X.; Ding, K.; Liu, J.; Wang, Z.; Tang, R.; Xue, L.; Wang, H.; Zhang, Q.; Tan, Z.-M.; Fu, C.; Davis, S. J.; Andreae, M. O.; Ding, A. Smoke-weather interaction affects extreme wildfires in diverse coastal regions. *Science* **2023**, *379* (6631), 457−461.
(50) Baboomian, V. J.; He, Q.; Montoya-Aguilera, J.; Ali, N.; Fleming, L. T.; Lin, P.; Laskin, A.; Laskin, J.; Rudich, Y.; Nizkorodov, S. A. Light absorption and scattering properties of indole secondary organic aerosol prepared under various oxidant and relative humidity conditions. *Aerosol Sci. Technol.* **2023**, *57* (6), 532−545.
(51) Dennison, P. E.; Charoensiri, K.; Roberts, D. A.; Peterson, S. H.; Green, R. O. Wildfire temperature and land cover modeling using hyperspectral data. *Remote Sens. Environ.* **2006**, *100* (2), 212−222.
(52) Strand, T.; Larkin, N.; Rorig, M.; Krull, C.; Moore, M. PM2.5 measurements in wildfire smoke plumes from fire seasons 2005−2008 in the Northwestern United States. *J. Aerosol Sci.* **2011**, *42* (3), 143−155.
(53) Ding, Y.; Cruz, I.; Freedman, F.; Venkatram, A. Improving spatial resolution of PM2.5 measurements during wildfires. *Atmos. Pollut. Res.* **2021**, *12* (5), No. 101047.
(54) Junghenn Noyes, K. T.; Kahn, R. A.; Limbacher, J. A.; Li, Z. Canadian and Alaskan wildfire smoke particle properties, their evolution, and controlling factors, from satellite observations. *Atmos. Chem. Phys.* **2022**, *22* (15), 10267−10290.
(55) Bertram, A. K.; Martin, S. T.; Hanna, S. J.; Smith, M. L.; Bodsworth, A.; Chen, Q.; Kuwata, M.; Liu, A.; You, Y.; Zorn, S. R. Predicting the relative humidities of liquid-liquid phase separation, efflorescence, and deliquescence of mixed particles of ammonium sulfate, organic material, and water using the organic-to-sulfate mass ratio of the particle and the oxygen-to-carbon elemental ratio of the organic component. *Atmos. Chem. Phys.* **2011**, *11* (21), 10995−11006.
(56) Liu, T.; Huang, D. D.; Li, Z.; Liu, Q.; Chan, M.; Chan, C. K. Comparison of secondary organic aerosol formation from toluene on initially wet and dry ammonium sulfate particles at moderate relative humidity. *Atmos. Chem. Phys.* **2018**, *18* (8), 5677−5689.
(57) Atkinson, R.; Aschmann, S. M.; Carter, W. P. L. Kinetics of the reactions of O3 and OH radicals with furan and thiophene at 298 ± 2 K. *Int. J. Chem. Kinet.* **1983**, *15* (1), 51−61.
(58) Atkinson, R.; Aschmann, S. M.; Winer, A. M.; Carter, W. P. L. Rate constants for the gas phase reactions of OH radicals and O3 with pyrrole at 295 ± 1 K and atmospheric pressure. *Atmos. Environ.* **1984**, *18* (10), 2105−2107.
(59) Atkinson, R.; Aschmann, S. M.; Winer, A. M.; Carter, W. P. L. Rate constants for the gas-phase reactions of nitrate radicals with furan, thiophene, and pyrrole at 295. +-. 1 K and atmospheric pressure. *Environ. Sci. Technol.* **1985**, *19* (1), 87−90.
(60) Bahreini, R.; Keywood, M. D.; Ng, N. L.; Varutbangkul, V.; Gao, S.; Flagan, R. C.; Seinfeld, J. H.; Worsnop, D. R.; Jimenez, J. L. Measurements of Secondary Organic Aerosol from Oxidation of Cycloalkenes, Terpenes, and m-Xylene Using an Aerodyne Aerosol Mass Spectrometer. *Environ. Sci. Technol.* **2005**, *39* (15), 5674−5688.
(61) Lopez-Hilfiker, F. D.; Mohr, C.; Ehn, M.; Rubach, F.; Kleist, E.; Wildt, J.; Mentel, T. F.; Lutz, A.; Hallquist, M.; Worsnop, D.; Thornton, J. A. A novel method for online analysis of gas and particle composition: description and evaluation of a Filter Inlet for Gases and AEROsols (FIGAERO). *Atmos. Meas. Technol.* **2014**, *7* (4), 983−1001.
(62) Frisch, M. J.; Trucks, G. W.; Schlegel, H. B.; Scuseria, G. E.; Robb, M. A.; Cheeseman, J. R.; Scalmani, G.; Barone, V.; Petersson, G. A.; Nakatsuji, H.; Li, X.; Caricato, M.; Marenich, A. V.; Bloino, J.; Janesko, B. G.; Gomperts, R.; Mennucci, B.; Hratchian, H. P.; Ortiz, J. V.; Izmaylov, A. F.; Sonnenberg, J. L.; Williams; Ding, F.; Lipparini, F.; Egidi, F.; Goings, J.; Peng, B.; Petrone, A.; Henderson, T.; Ranasinghe, D.; Zakrzewski, V. G.; Gao, J.; Rega, N.; Zheng, G.; Liang, W.; Hada, M.; Ehara, M.; Toyota, K.; Fukuda, R.; Hasegawa, J.; Ishida, M.; Nakajima, T.; Honda, Y.; Kitao, O.; Nakai, H.; Vreven, T.; Throssell, K.; Montgomery, J. A., Jr.; Peralta, J. E.; Ogliaro, F.; Bearpark, M. J.; Heyd, J. J.; Brothers, E. N.; Kudin, K. N.; Staroverov, V. N.; Keith, T. A.; Kobayashi, R.; Normand, J.; Raghavachari, K.; Rendell, A. P.; Burant, J. C.; Iyengar, S. S.; Tomasi, J.; Cossi, M.; Millam, J. M.; Klene, M.; Adamo, C.; Cammi, R.; Ochterski, J. W.; Martin, R. L.; Morokuma, K.; Farkas, O.; Foresman, J. B.; Fox, D. J. *Gaussian 16,* Rev. C.01; Gaussian, Inc.: Wallingford, CT, 2016.
(63) Becke, A. D. Density-functional exchange-energy approximation with correct asymptotic behavior. *Phys. Rev. A* **1988**, *38* (6), 3098−3100.
(64) Stephens, P. J.; Devlin, F. J.; Chabalowski, C. F.; Frisch, M. J. Ab Initio Calculation of Vibrational Absorption and Circular Dichroism Spectra Using Density Functional Force Fields. *J. Phys. Chem.* **1994**, *98* (45), 11623−11627.
(65) Ditchfield, R.; Hehre, W. J.; Pople, J. A. Self-Consistent Molecular-Orbital Methods. IX. An Extended Gaussian-Type Basis for Molecular-Orbital Studies of Organic Molecules. *J. Chem. Phys.* **1971**, *54* (2), 724−728.
(66) Jacquemin, D.; Perpète, E. A.; Scuseria, G. E.; Ciofini, I.; Adamo, C. TD-DFT Performance for the Visible Absorption Spectra of Organic Dyes: Conventional versus Long-Range Hybrids. *J. Chem. Theory Comput.* **2008**, *4* (1), 123−135.
(67) Chen, J. Y.; Rodriguez, E.; Jiang, H.; Chen, K.; Frie, A.; Zhang, H.; Bahreini, R.; Lin, Y.-H. Time-Dependent Density Functional Theory Investigation of the UV−Vis Spectra of Organonitrogen Chromophores in Brown Carbon. *ACS Earth Space Chem.* **2020**, *4* (2), 311−320.
(68) Mennucci, B.; Cammi, R.; Tomasi, J. Excited states and solvatochromic shifts within a nonequilibrium solvation approach: A new formulation of the integral equation formalism method at the self-consistent field, configuration interaction, and multiconfiguration self-consistent field level. *J. Chem. Phys.* **1998**, *109* (7), 2798−2807.
(69) Shiraiwa, M.; Yee, L. D.; Schilling, K. A.; Loza, C. L.; Craven, J. S.; Zuend, A.; Ziemann, P. J.; Seinfeld, J. H. Size distribution dynamics reveal particle-phase chemistry in organic aerosol formation. *Proc. Natl. Acad. Sci. U.S.A.* **2013**, *110* (29), 11746−11750.

(70) Hamed, A.; Korhonen, H.; Sihto, S.-L.; Joutsensaari, J.; Järvinen, H.; Petäjä, T.; Arnold, F.; Nieminen, T.; Kulmala, M.; Smith, J. N.; Lehtinen, K. E. J.; Laaksonen, A. The role of relative humidity in continental new particle formation. *J. Geophys. Res. Atmos.* **2011**, *116*, No. D03202.
(71) Kampf, C. J.; Jakob, R.; Hoffmann, T. Identification and characterization of aging products in the glyoxal/ammonium sulfate system - implications for light-absorbing material in atmospheric aerosols. *Atmos. Chem. Phys.* **2012**, *12* (14), 6323−6333.
(72) Aiona, P. K.; Lee, H. J.; Leslie, R.; Lin, P.; Laskin, A.; Laskin, J.; Nizkorodov, S. A. Photochemistry of Products of the Aqueous Reaction of Methylglyoxal with Ammonium Sulfate. *ACS Earth Space Chem.* **2017**, *1* (8), 522−532.
(73) Huang, M.; Zhang, J.; Cai, S.; Liao, Y.; Zhao, W.; Hu, C.; Gu, X.; Fang, L.; Zhang, W. Characterization of particulate products for aging of ethylbenzene secondary organic aerosol in the presence of ammonium sulfate seed aerosol. *J. Environ. Sci.* **2016**, *47*, 219−229.
(74) Grace, D. N.; Sharp, J. R.; Holappa, R. E.; Lugos, E. N.; Sebold, M. B.; Griffith, D. R.; Hendrickson, H. P.; Galloway, M. M. Heterocyclic Product Formation in Aqueous Brown Carbon Systems. *ACS Earth Space Chem.* **2019**, *3* (11), 2472−2481.
(75) Lian, X.; Zhang, G.; Yang, Y.; Lin, Q.; Fu, Y.; Jiang, F.; Peng, L.; Hu, X.; Chen, D.; Wang, X.; Peng, P. a.; Sheng, G.; Bi, X. Evidence for the Formation of Imidazole from Carbonyls and Reduced Nitrogen Species at the Individual Particle Level in the Ambient Atmosphere. *Environ. Sci. Technol. Lett.* **2021**, *8* (1), 9−15.
(76) Cao, G.; Yan, Y.; Zou, X.; Zhu, R.; Ouyang, F. Applications of Infrared Spectroscopy in Analysis of Organic Aerosols. *Spectr. Anal. Rev.* **2018**, *06*, 12−32.
(77) Saleh, R. From Measurements to Models: Toward Accurate Representation of Brown Carbon in Climate Calculations. *Curr. Pollut. Rep.* **2020**, *6* (2), 90−104.
(78) Joo, T.; Machesky, J. E.; Zeng, L.; Hass-Mitchell, T.; Weber, R. J.; Gentner, D. R.; Ng, N. L. Secondary Brown Carbon Formation From Photooxidation of Furans From Biomass Burning. *Geophys. Res. Lett.* **2024**, *51* (1), No. e2023GL104900.
(79) Nguyen, T. B.; Lee, P. B.; Updyke, K. M.; Bones, D. L.; Laskin, J.; Laskin, A.; Nizkorodov, S. A. Formation of nitrogen- and sulfur-containing light-absorbing compounds accelerated by evaporation of water from secondary organic aerosols. *J. Geophys. Res. Atmos.* **2012**, *117*, No. D01207.
(80) Nguyen, T. B.; Laskin, A.; Laskin, J.; Nizkorodov, S. A. Brown carbon formation from ketoaldehydes of biogenic monoterpenes. *Faraday Discuss.* **2013**, *165* (0), 473−494.
(81) Lin, P.; Liu, J.; Shilling, J. E.; Kathmann, S. M.; Laskin, J.; Laskin, A. Molecular characterization of brown carbon (BrC) chromophores in secondary organic aerosol generated from photo-oxidation of toluene. *Phys. Chem. Chem. Phys.* **2015**, *17* (36), 23312−23325.
(82) Mitra, K.; Mishra, H. R.; Pei, X.; Pathak, R. K. Secondary Organic Aerosol (SOA) from Photo-Oxidation of Toluene: 1 Influence of Reactive Nitrogen, Acidity and Water Vapours on Optical Properties. *Atmosphere* **2022**, *13* (7), 1099.
(83) Cho, C.; Kim, S.-W.; Choi, W.; Kim, M.-H. Significant light absorption of brown carbon during the 2020 California wildfires. *Sci. Total Environ.* **2022**, *813*, No. 152453.
(84) Kodros, J. K.; Papanastasiou, D. K.; Paglione, M.; Masiol, M.; Squizzato, S.; Florou, K.; Skyllakou, K.; Kaltsonoudis, C.; Nenes, A.; Pandis, S. N. Rapid dark aging of biomass burning as an overlooked source of oxidized organic aerosol. *Proc. Natl. Acad. Sci. U.S.A.* **2020**, *117* (52), 33028.
(85) Schnitzler, E. G.; Gerrebos, N. G. A.; Carter, T. S.; Huang, Y.; Heald, C. L.; Bertram, A. K.; Abbatt, J. P. D. Rate of atmospheric brown carbon whitening governed by environmental conditions. *Proc. Natl. Acad. Sci. U.S.A.* **2022**, *119* (38), No. e2205610119.
(86) Wong, J. P. S.; Nenes, A.; Weber, R. J. Changes in Light Absorptivity of Molecular Weight Separated Brown Carbon Due to Photolytic Aging. *Environ. Sci. Technol.* **2017**, *51* (15), 8414−8421.
(87) Wong, J. P. S.; Tsagkaraki, M.; Tsiodra, I.; Mihalopoulos, N.; Violaki, K.; Kanakidou, M.; Sciare, J.; Nenes, A.; Weber, R. J. Atmospheric evolution of molecular-weight-separated brown carbon from biomass burning. *Atmos. Chem. Phys.* **2019**, *19* (11), 7319−7334.
(88) Shetty, N.; Liu, P.; Liang, Y.; Sumlin, B.; Daube, C.; Herndon, S.; Goldstein, A. H.; Chakrabarty, R. K. Brown carbon absorptivity in fresh wildfire smoke: associations with volatility and chemical compound groups. *Environ. Sci. Atmos.* **2023**, *3* (9), 1262−1271.


https://doi.org/10.1021/acsestair.4c00025
*ACS EST Air* 2024, 1, 426−437